

Mechanics of viscous wedges: Modeling by analytical and numerical approaches

Sergei Medvedev

Department of Oceanography, Dalhousie University, Halifax, Nova Scotia, Canada

Received 10 January 2001; revised 25 November 2001; accepted 30 November 2001; published 26 June 2002.

[1] Although complex rheological models have been used to study the evolution of orogenic wedges, many features of simple models remain to be fully explained. Here, we analyze the plane strain evolution of model orogenic wedges under simple boundary and rheological conditions. The uniform linear viscosity wedge is driven by motion of a basal boundary at a constant velocity. Three main analysis techniques are used: analytical (algebraic analysis of scales involved), semianalytical (thin sheet approximation), and a complete numerical approach. Application of this variety of approaches provides a better understanding of the underlying physics and outlines the advantages and disadvantages of the different techniques. The evolution of wedges can be divided into three phases. Initially, wedge growth is mainly vertical and symmetrical and depends little on the viscosity. The second phase exhibits almost self-similar growth with the appearance of surface extension, within an otherwise compressional system, and development of asymmetry. The last phase involves widening of wedge and further development of asymmetry and surface extension, the average slope of wedge decreases during this phase. The Ramberg number, the ratio of characteristic gravitational to shear stress, defines the duration of each phase. Several parameters introduced here (mean surface slope, asymmetry of the wedge, surface extension, and near-surface strain history) allow observations from natural wedges to be linked to the bulk viscosity of the model wedges. Analysis shows that the thin sheet approximation does not correctly describe the initial stages of wedge evolution. *INDEX TERMS*: 8020 Structural Geology: Mechanics; 8102 Tectonophysics: Continental contractional orogenic belts; 8122 Tectonophysics: Dynamics, gravity and tectonics; 8164 Tectonophysics: Stresses—crust and lithosphere; *KEYWORDS*: orogenic wedge, thin-sheet approximation, numerical modelling, scaling analysis, extension, contraction

1. Introduction

[2] The behavior of viscous models of the lithosphere in the context of plate tectonic convergence provides some insights into the dynamics of the growth of orogenic wedges. In previous work, viscous material has been used in analogue models [Buck and Sokoutis, 1994] and various numerical [Ellis et al., 1995; Royden, 1996; Willett, 1999; Shen et al., 2001] and analytical [Emerman and Turcotte, 1983; Platt, 1986, 1993, 2000; Buck and Sokoutis, 1994; Ellis, 1996] investigations. Several interpretations based on field studies of accretionary prisms emphasize the relevance of the viscous model for the internal deformation of wedges [Ring and Brandon, 1999; Feehan and Brandon, 1999]. Buck and Sokoutis [1994], Royden [1996], and Willett [1999] demonstrated that a uniform linear-viscous orogenic wedge can exhibit surface extension as the result of the convergent basal boundary motion, which may explain

normal sense shear features of several orogenic zones (see examples from Willett [1999]).

[3] Even though many studies have modeled the evolution of orogenic wedges using more complex rheologies [e.g., Beaumont et al., 1994, 1996, 2000; Ellis et al., 1998], some features of the underlying simple models remain unclear. The purpose of present work is to improve our understanding of the behavior of uniform linear viscous wedges by identifying analytically the key parameters controlling their growth.

[4] The boundary and initial conditions for the formation of an asymmetric doubly-vergent wedge (Figure 1a) were chosen for analysis owing to their simplicity and because they are the same as those used by Buck and Sokoutis [1994] and Willett [1999]. By choosing uniform linear viscosity and time-invariant boundary conditions we limit the problem to only a few free parameters listed in the first part of Table 1.

[5] In simplifying the model some processes that accompany orogenesis, such as isostasy and erosion, have been neglected. The time range at which the approach can be used is also limited. The boundary conditions chosen also

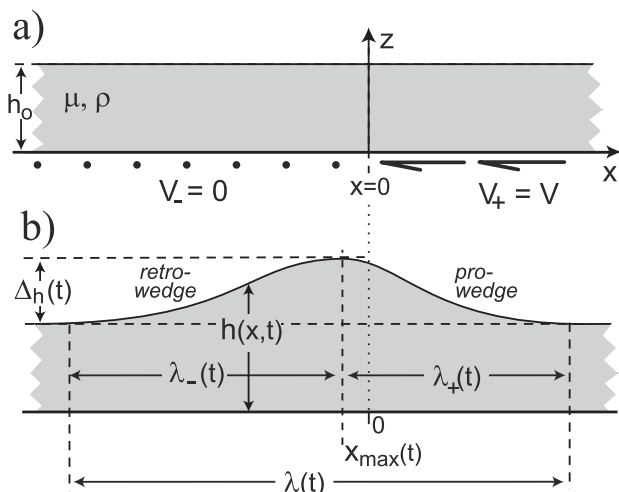


Figure 1. (a) Basic wedge model. Initial and boundary conditions include stress-free upper surface and basal velocity, $V(x)$, which is constant (V_+ or V_-) and has singularity at $x = 0$. The base is horizontal and fixed. Lateral boundaries extend beyond the deformation. Initial layer thickness is h_0 , and layer material has constant viscosity, μ , and density, ρ (Table 1). (b) Deformed wedge. Length scale of deformation, λ , is divided to λ_+ and λ_- representing scales for two sides of the wedge; wedge shape is measured by thickness, $h(x, t)$, and maximum uplift, $\Delta_h = \max(h - h_0)$ located at x_{\max} . See Table 1 for other parameters.

preclude direct application of this model to accretionary wedges, where a basal decollement and/or rear backstop significantly influence the evolution [e.g., Platt, 1993]. Although the complexities of natural systems restrict direct quantitative comparison with the model results, qualitative similarities exist [e.g., Royden, 1996; Willett, 1999].

[6] We investigate the evolution of several wedge properties that can be compared directly to geological observations and data, such as shape of the wedge (rate of growth, average slopes, and asymmetry), and the instantaneous and finite surface strains (Figure 1b and Table 1). Several approaches are used for analysis and modeling:

1. Scaling analysis roughly estimates forces acting in the system and the mass balance. Two analytical models are presented in this work: AM1 (section 2.1) and AM2/AM2h (section 3.4).

2. Details of the evolution cannot be obtained analytically; therefore numerical models are needed. The simplest possible numerical model is based on the thin sheet approximation, the SS approach (“simple shear,” following classification presented by Medvedev and Podladchikov [1999a]). Although this approach has been used before to describe orogenesis [Emerman and Turcotte, 1983; Lobkovsky and Kerchman, 1991; Buck and Sokoutis, 1994], some new insights into this approach are discussed here (section 2.2).

3. The results and conclusions based on the approximate techniques listed above are tested by reference to a more complete numerical model based on the finite element approach containing the complete balance of forces, the PS approach (“plane strain” [Fallsack, 1995], section 2.3).

[7] Application of these different approaches not only provides a better understanding the physical processes controlling the evolution of wedges but also allows insight into the limitations of different approaches. The main emphasis here is on the SS approach, which is widely used in geodynamics. However, the major simplifications implicit in this method require a more systematic investigation of the consequent limitations and applicability than has been done to date [Royden, 1996; Medvedev and Podladchikov, 1999a, 1999b].

[8] The first part of the paper presents approaches used to investigate the model. The second part concerns the evolution of wedge shape and classification of the different phases of evolution. The third part presents the evolution of surface strains and strain rates.

2. Methods

2.1. Analytical Model (AM1): Scaling Analysis

[9] The model described here is based on rough estimations of forces and mass balance. The horizontal force balance in the wedge for the case of a horizontal base and stress-free upper surface is

$$-F_1 + F_2 - F_\tau = 0, \quad (1)$$

where the forces are shown on Figure 2. The forces in equation (1) can be estimated from the bulk stresses in the wedge:

$$\begin{aligned} F_1 &= \int_0^{h_0} \sigma_{xx}|_{x=\infty} dz \sim \frac{1}{2} \rho g h_0^2, \\ F_2 &= \int_0^{h_0 + \Delta_h} \sigma_{xx}|_{x=0} dz \sim \frac{1}{2} \rho g (h_0 + \Delta_h)^2 + 2\mu \frac{V}{\lambda} \tilde{h}, \\ F_\tau &= \int_0^{x_1} \sigma_{xz}|_{z=0} dx \sim \frac{1}{2} \mu \frac{V}{h} \lambda, \end{aligned} \quad (2)$$

where indexed σ denotes the components of the stress tensor and $\tilde{h} = h_0 + 0.5\Delta_h$ is the average thickness of the wedge assuming a triangular geometry. The averaged horizontal strain rate can be estimated as V/λ , which is then used to estimate the viscous part of F_2 .

[10] An estimation of basal shear stress used in the expression for F_τ is made as follows. First, the averaged vertical variation of horizontal velocity was estimated as a difference between basal velocity, V , and the average velocity at the top surface of the prowedge ($V/2$). This variation divided by averaged thickness of wedge, \tilde{h} , and multiplied by viscosity results in averaged shear stress in the prowedge. As shear stress is zero at the top surface, the shear stress along the base can be estimated as twice the average.

[11] Substitution of equation (2) into equation (1) gives

$$\rho g \Delta_h \tilde{h} + 2\mu V \frac{\tilde{h}}{\lambda} - \frac{1}{2} \mu \frac{V \lambda}{\tilde{h}} = 0, \quad (3)$$

or

$$F_g + F_n - F_\tau = 0,$$

Table 1. Parameters of the Viscous Wedge Problem

Parameter	Definition, Comments	SI Units [Dimensional Scale]	Variations Analyzed [Range of Results]
<i>Setup Parameters</i>			
H^*	length scale, $H^* = h_0$	m	5–40 km
g	acceleration due to gravity	m/s^2	10 m/s^2
V^*	velocity, $V^* = \text{abs}(V_+ - V_-)$	m/s	0.1–4 cm/yr
μ^*	viscosity	Pa s	$10^{20} - 10^{23} \text{ Pa s}$
ρ^*	density	kg/m^3	$(2-3.3) \times 10^3 \text{ kg/m}^3$
<i>Characteristic Values</i>			
σ_g^*	gravitational stress	Pa	$\rho^* g H^*$
σ_τ^*	shear stress	Pa	$\mu^* V^* / H^*$
σ_n^*	normal stress	Pa	$\mu^* V^* / \lambda$
t^*	convergence time, time needed to converge the system by horizontal distance of one characteristic length scale (H^*)	s	H^* / V^*
t_e^*	evolution time (equation (12))	s	$\sqrt{\mu^* / \rho^* g V^*}$
<i>Dimensionless Complexes</i>			
$Rm = \sigma_g^* / \sigma_\tau^*$	Ramberg number, ratio of gravity to shear stresses (equation (4), Table 2)	–	1–20
$Ar = \sigma_g^* / \sigma_n^*$	Argand number, ratio of gravity to normal stresses	–	–
<i>Variables^a</i>			
$h(x, t)$	actual thickness of the layer (Figure 1b)	$[H^*]$	[1–3]
$L(t)$	width of zone of finite extension along the top surface (Figure 11b)	$[H^*]$	[0–5]
t	dimensional time	$[t^*], [t_e^*]$	–
$t' = t/t^*$	dimensionless time corresponding to the total convergence in units of the initial thickness h_0	–	0–30
$t'_e = t/t_e^*$	dimensionless time corresponding to stages of evolution (equation (12), Figure 14)	–	0–30
$V(x)$	basal velocity: $V = 0$ for $x < 0$ and $V = -V^*$ for $x > 0$ (Figure 1a)	$[V^*]$	0– V^*
$x_{\text{max}}(t)$	horizontal position of maximum uplift of wedge (Figure 7b)	$[H^*]$	[0–1]
$\tilde{\alpha}(t)$	tangent of mean slope of wedge (equation (11), Figure 5)	–	[0–0.3]
$\Delta_h(t)$	maximum uplift in the system, $\max(h - h_0)$ (Figure 3b and 3d)	$[H^*]$	[0–2]
$\varepsilon(x, t)$	surface strain, positive ε indicates finite extension	–	[up to 100%]
$\varepsilon(i, t)$	strain evolution of certain, i th, Lagrangian element (Figure 12)	–	[up to 100%]
λ	width of wedge, horizontal length scale of deformation (equation (6))	$[H^*]$	[2–80]
$\lambda_+(t), \lambda_-(t)$	widths of prowedge and retrowedge, $\lambda_+ + \lambda_- = \lambda$ (Figure 7a)	$[H^*]$	–

^aDimensionless variables are marked by primes. They can be rescaled to dimensional equivalents by multiplying by the dimensional scales from this table.

where F_g approximates the gravity forces acting in the wedge (this term relates to the gradient of potential energy [Jones *et al.*, 1996]); F_n estimates the influence of horizontal compressional viscous stresses in the system due to advection of mass into the wedge; and F_τ represents shear stresses acting along the base of the wedge. The dimensionless ratio, the Ramberg number [after Ramberg, 1981; Weijemars and Schmeling, 1986],

$$Rm = \rho g h_0^2 / \mu V \quad (4)$$

is used to relate gravitational stresses acting in the model to the basal shear stress (see Table 1). Elsewhere, this ratio was termed the Argand number in other basally driven wedge problems [Buck and Sokoutis, 1994; Willett, 1999]. However, the Argand number was introduced by England and McKenzie [1982] as ratio of gravitational (buoyancy) to horizontal compressional stresses, not shear stresses. Rm is used here to distinguish the difference in the physics behind these numbers. To illustrate this difference, we also construct the Argand number (Table 1) according to the England and McKenzie [1982] definition, but it is related to a horizontal length scale λ , which cannot be readily estimated from the initial and/or boundary conditions and in further developments we do not refer to values of Ar .

[12] The range of values of Rm used in the further analyses is illustrated in Table 2. Values of Rm higher than 20 result in very wide wedges, while geological situations with Rm lower than 1 are unlikely. We now scale all parameters to be dimensionless using the scales

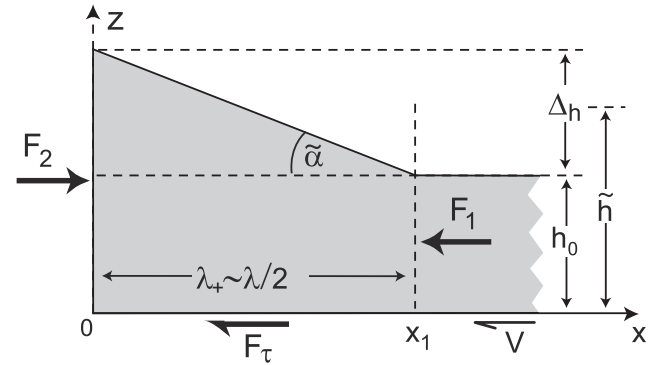


Figure 2. Horizontal forces acting on the prowedge. Wedge is assumed to be geometrically symmetric ($\lambda_+ \sim \lambda_- \sim \lambda/2$). Region $x \geq x_1$ is undeformed; therefore no viscous stresses contribute to force F_1 . Average thickness of the wedge is $\tilde{h} \sim h_0 + \Delta h/2$, and mean slope is $\tilde{\alpha} = \Delta h / \lambda_+$.

Table 2. Limiting Parameter Values Used to Calculate Range of Rm

	Rm	ρ , kg/m ³	h_0 , km	V , cm/yr	μ , Pa s
Strong crust	1	3100	35	1	10 ²³
Sediments	20	2800	5	1	10 ²⁰

presented in the Table 1. For example, the averaged thickness of the wedge becomes $\bar{h}' = 1 + \Delta_h'/2$. Equation (3) then becomes

$$Rm \frac{\Delta_h'}{\lambda'} + \frac{2}{(\lambda')^2} - \frac{1}{2(\bar{h}')^2} = 0, \quad (5)$$

demonstrating the control of the force balance by Rm .

[13] Assuming that the wedge has a triangular shape, the total mass balance can be expressed in dimensional and [dimensionless] forms:

$$\Delta_h \lambda / 2 \sim t V h_0, \quad [\Delta_h' \lambda' / 2 \sim t'] \quad (6)$$

where dimensionless time t' characterizes the amount of advected material (see Table 1). The system of equations (5) and (6) for the first analytical model, AM1, has two unknowns, $\lambda(t)$ and $\Delta_h(t)$ that can be calculated analytically and used to predict the evolution of the most general properties such as height and width of the wedge, and averaged forces acting in the wedge (see section 3.3 and section 4.2). The main limitation of AM1 is that the geometry and boundary conditions are symmetric about $x = 0$.

2.2. Thin Sheet Approximation (Model SS): Semianalytical Approach

[14] Semianalytical methods used to investigate the evolution of a wedge include so-called thin sheet approximations. These models attempt to calculate analytically the vertical distributions of stresses based on the geometric assumption that the ratio of the vertical to horizontal length scales in the model is small.

[15] The SS (“simple shear”) approach is based on the lubrication approximation to the Stokes equations. Applied to the problem of this work, Stokes equations of motion in dimensionless form give

$$Rm \frac{\partial P'}{\partial x'} - \frac{\partial^2 v_x'}{\partial (z')^2} - \left[\frac{\partial^2 v_x'}{\partial (x')^2} \right] = 0$$

$$Rm \left(\frac{\partial p'}{\partial z'} + 1 \right) - \left[\frac{\partial^2 v_z'}{\partial (x')^2} + \frac{\partial^2 v_z'}{\partial (z')^2} \right] = 0, \quad (7)$$

where primes indicate dimensionless values (Table 1), P is the pressure, and $v_x(x, z)$ and $v_z(x, z)$ are horizontal and vertical velocities. Scaling the mass forces (ρg) in the second equation results in the “1.” The SS approach assumes that variations in the horizontal direction are much smaller than in the vertical direction and that the vertical velocity is smaller than horizontal velocity. This results in neglecting

the terms in brackets, which means neglecting the normal viscous stresses in the horizontal balance of forces and assuming pressure to be lithostatic (see complete asymptotic analysis by *Zanemonetz et al.* [1976]; *Lobkovsky and Kerchman* [1991]; *Medvedev* [1993]; and *Medvedev and Podladchikov* [1999b]). After omitting terms in brackets, equations (7) represent the lubrication approximation [*Schlichting*, 1979; *Emerman and Turcotte*, 1983]. Integration of the simplified equations (7) gives a parabolic variation of horizontal velocity with depth:

$$v_x'(x', z') = V' - Rm \frac{z'(2h' - z')}{2} \frac{\partial h'}{\partial x'}; \quad (8)$$

see Table 1 for definition of terms. Combining the integrated velocity profile with mass conservation results in a simple description of wedge evolution by a single equation [e.g., *Buck and Sokoutis*, 1994]:

$$\frac{\partial h'}{\partial t'} + \frac{\partial}{\partial x'} (V' h') - Rm \frac{\partial}{\partial x'} \left(\frac{(h')^3}{3} \frac{\partial h'}{\partial x'} \right) = 0. \quad (9)$$

Note that the form of the SS approach presented by equations (8) and (9) assumes a fixed, flat base ($z = 0$). The essence of the physics behind this approach is that the gravitational spreading of the wedge is balanced by the shear stress in the layer.

[16] Our analytical model AM1 (section 2.1, equation (5)) includes three types of forces in the balance; gravitational, normal viscous, and shear viscous. The SS approach neglects normal viscous stresses. Thus AM1 can be recognized as more complete qualitatively but cannot handle any detailed analysis. Numerical treatment based on the SS approach can give detailed results, but the implications of the assumptions behind this approach should be tested. The SS approximation is believed to be acceptable if the horizontal length scale of the problem is much greater than the vertical scale [*Zanemonetz et al.*, 1976; *Medvedev*, 1993]. In the next sections we will investigate the accuracy of this assumption.

2.3. Numerical Approach: Plane Strain Finite Element Method (PS)

[17] This method is based on the finite element discretization of the complete balance of forces, its formulation does not imply any simplifying assumptions. Therefore this method is used as a reference, and all our conclusions have been tested against this approach.

[18] The numerical code involves an arbitrary Lagrangian-Eulerian formulation. The finite element calculation of velocities is performed on an Eulerian grid that undergoes little distortion as the wedge grows. The Lagrangian grid is used to track deformations and to advect material properties [*Fullsack*, 1995]. This code [*Fullsack*, 1995] has been tested and used extensively [e.g., *Beaumont et al.*, 1994, 1996, 2000; *Willett*, 1999]. Several types of finite element interpolations (e.g., bilinear 4 nodes, quadratic 9 nodes, Crouzeix-Raviart 7 nodes and Pian-Sumihara 4 nodes [*Cuvelier et al.*, 1986; *Zienkiewicz and Taylor*, 1989]) have been implemented and tested against analytical solutions, and results for different elements were compared to ensure

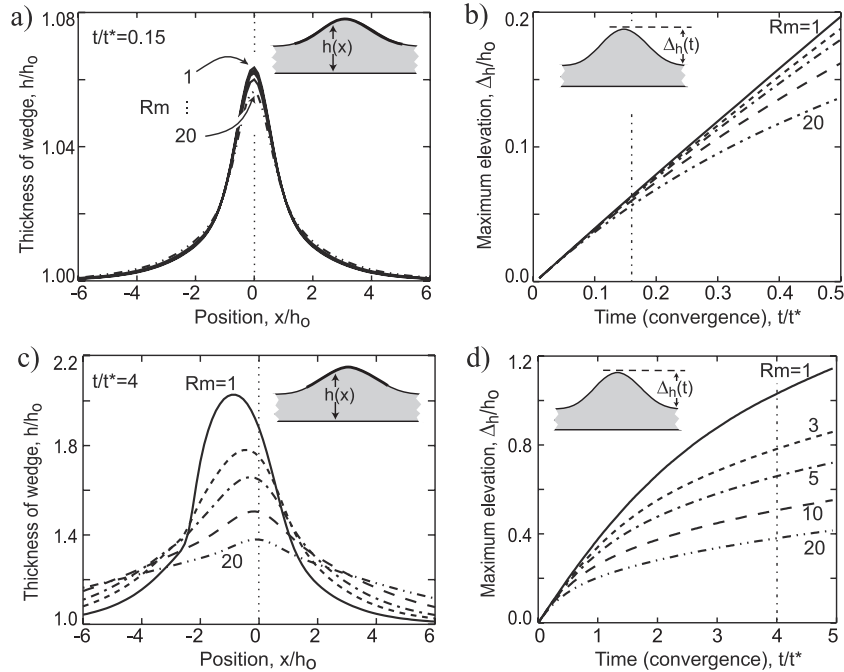


Figure 3. Topography and thickness of wedges with different Rm . In the initial phase (Figures 3a and 3b) the dependence on Rm is low, which contrasts with the later phases (Figures 3c and 3d). (a and c) Nondimensional topography versus position at nondimensional time shown by dashed line (Figures 3b and 3d). (b and d) Normalized maximum elevation versus time. Note vertical exaggeration (Figures 3a and 3c).

correctness (P. Fullsack, personal communications, 1999–2000).

3. Results

[19] Results presented here are the solutions for the problem described by Figure 1 for the asymmetric doubly-vergent wedge. The ideas and solutions of analytical (AM1 and AM2) and semianalytical (SS) approaches are tested by comparison with numerical results of the full finite element approach (PS). Figures present results obtained by the PS approach unless otherwise specified.

3.1. Evolution of Wedge Shape: Dependence on Rm

[20] Initially, for small uplift ($\Delta_h \ll h_0$), equation (5) concludes that λ is neither much smaller nor much greater than h_0 and that the first term of equation (5) is much smaller than the other two. Thus the solution is only weakly dependent on Rm . This conclusion is supported by the PS numerical results (Figures 3a and 3b). This initial stage is shorter the larger the Rm (equation (5)), and it can be seen (Figures 3b and 3d) that the results are distinct for the range of Rm used here when $t' \sim 0.4$, where t' (Table 1) is the dimensionless time. More evolved models (Figures 3c and 3d) exhibit large differences in styles depending on Rm .

[21] The width of deformation can be estimated by $\lambda'(t) \approx 2t'/\Delta_h'$ (equation (6)) using Figures 3b and 3d. This gives $\lambda \sim 5h_0$ for the initial stage ($t' = 0.1$ to 0.3) independent of Rm and with a very low dependence on time (Figure 3a). During the later stages the width, λ , varies with time and

Rm . For example, the width ranges from $8h_0$ to $25h_0$ at $t' = 4$ depending on Rm (Figure 3c).

3.2. Comparison With Thin Sheet Approximations

[22] In this section we compare results of the complete PS modeling approach with results obtained by the SS thin sheet approximation and analyze this comparison using other approaches. The accuracy of thin sheet approximations is directly related to the smallness of the vertical to horizontal length-scale ratio [Zanamonetz *et al.*, 1976; Medvedev, 1993], which is usually defined by the initial and/or boundary conditions of a problem. However, the problem considered here does not have predefined horizontal length scale (Figure 1a). To estimate the accuracy, we compare the AM1 and SS approaches. The term neglected by the SS approach in the horizontal balance of forces (equations (7)) corresponds to the term F_n from the integrated balance included in the AM1 approach (equation (5)). Dividing equation (5) by F_n and using the dimensionless form of equation (6) gives the following form of the horizontal force balance:

$$\frac{1}{2} Rm t' + 1 - \left(\lambda' / 2\tilde{h}' \right)^2 = 0 \quad (10)$$

Here the term neglected by the SS approach appears as “1,” and therefore the SS approximation can be valid only if both the first and the third terms in equation (10) are much greater than 1. The latter condition corresponds to the traditional criteria for thin sheet approximations that the width of deformation is much larger than the height. However, this condition applies to the results of finite

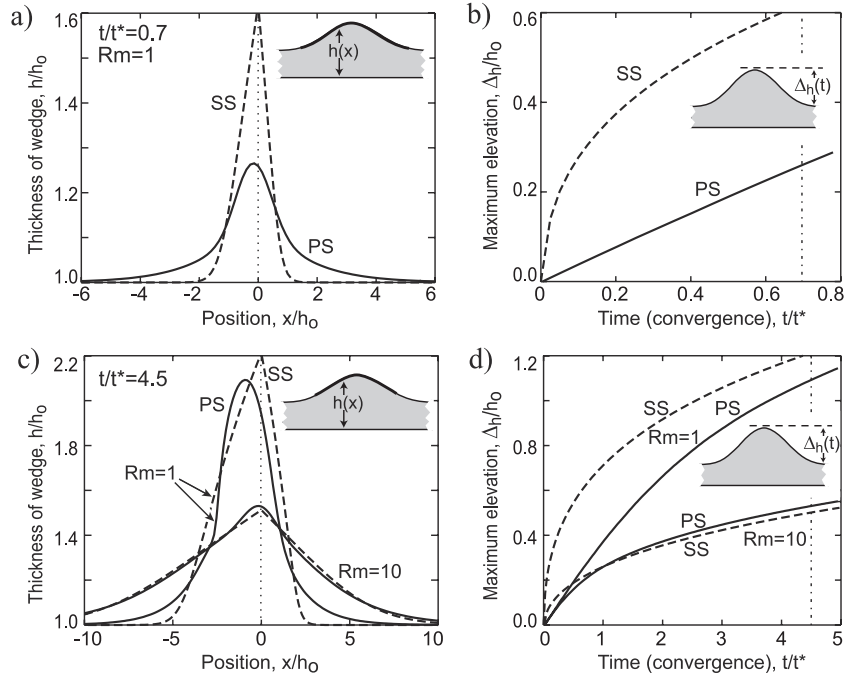


Figure 4. Comparison of wedge results obtained by the PS (solid line) and SS (dashed line) approaches for different phases of convergence: (a and b) initial and (c and d) developed shown as in Figure 3. For $Rm = 1$ the SS approach at the initial stages (Figures 4a and 4b) is inaccurate, while it improves for larger $t' = t/t^*$ (Figures 4c and 4d). Accuracy of SS also depends on Rm : higher values give better agreement with accurate PS solutions (Figures 4c and 4d). Note also that in the SS solution the point of maximum uplift is always at $x = 0$, while the PS solution demonstrates retroward shift.

deformation and these length scales are not predefined. The ratio λ'/h' does, however, grow with time and the accuracy of thin sheet approximation therefore increases (see comparison for $Rm = 1$ on Figure 4d).

[23] The condition $Rm t' \gg 1$ also results in accuracy increasing with time but requires special consideration during the initial phase. When $t' \sim 0$, the SS approximation is inaccurate because the first term of equation (10) is also ~ 0 . This phase is, however, short for high Rm . Hence the accuracy is poor for low Rm ($Rm = 1$, Figures 4a, 4b, and 4d) but is good for large Rm ($Rm = 10$, Figures 4c and 4d; see also comparison of the SS approach with an analogue experiment of *Buck and Sokoutis* [1994] where $Rm = 10$).

3.3. Evolution of Mean Slope

[24] How slopes of the wedge evolve with convergence is a characteristic property of the wedge. Investigations in this section are based on the “mean slope,” $\tilde{\alpha}$, of the wedge; defined as the ratio of the characteristic uplift of the system, Δ_h , to half of the characteristic width, $\lambda/2$ (Figures 2 and 5a). Using equation (6), $\tilde{\alpha}$ can be estimated for a symmetric wedge by

$$\tilde{\alpha} = \frac{\Delta_h}{\lambda/2} = \frac{(\Delta_h')^2}{t'} = \frac{\Delta_h^2}{th_0 V}. \quad (11)$$

Applying this equation to asymmetric wedges results results in $\tilde{\alpha}$ as an average value of the two slopes in the wedge.

[25] For AM1, equations (5) and (6) can be used to estimate time dependence of the mean slope analytically. The result for $Rm = 1$ (Figure 5a) shows three phases: I, initially the wedge growth is mostly vertical, thereby increasing $\tilde{\alpha}$; II, wedge growth is almost self-similar with near constant $\tilde{\alpha}$; III, finally, the wedge spreads horizontally and $\tilde{\alpha}$ decreases.

[26] AM1 results predict that as Rm is increased, the maximum $\tilde{\alpha}$ is reached earlier (the same behavior is also shown by PS results, Figure 5b). The time when the slope is a maximum, t_{\max} , can be estimated with good accuracy from the empirical condition $t_{\max} \sqrt{Rm} \approx \text{const}$. This allows us to introduce the characteristic evolution time for the wedge, t_e^* , as

$$t_e^* = t^* / \sqrt{Rm} = \sqrt{\frac{\mu^*}{\rho^* g V^*}} \quad (12)$$

and the new dimensionless evolution time, $t_e = t' \sqrt{Rm}$. The robustness of the evolution time is illustrated by the fact that the scaled times of maximum slope (indicated by arrow heads on Figure 5c) for different Rm occur in the interval $t_e \approx 4.3-5.3$. Using the scaling parameters presented in Table 2, the corresponding dimensional time t_{\max} varies from ~ 1 Myr for “sediments” to ~ 10 Myr for “strong crust” models.

[27] The SS approach results in monotonically decreasing mean slope (Figure 5a, the initial part, for $t' < 2$, of this curve is out of scale of the graph). This slope can, however,

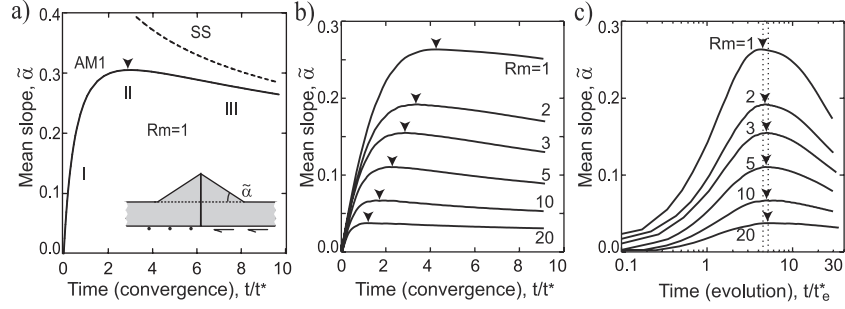


Figure 5. Mean slope, $\tilde{\alpha}$ (equation (11)), versus nondimensional time obtained by (a) AM1 and SS for $Rm = 1$, and (b and c) accurate numerical PS approach for different Rm . Three phases of growth (I–III) shown in Figure 5a. Points of maximum $\tilde{\alpha}$ shown by arrow heads. Figures 5b and 5c show corresponding results but for different scaling of time. The characteristic evolutionary time, t_e^* (equation (12)), depends on Rm and scaling by t_e^* aligns the time of maximum $\tilde{\alpha}$ for different Rm (compare Figures 5b and 5c).

be estimated analytically for the initial phases of evolution. The x integration of equation (9) over a small region across the discontinuity point, $x = 0$, in the limit that the width of the region of integration tends to zero, leads to the condition

$$\frac{\partial h}{\partial x} \Big|_{x=-0} - \frac{\partial h}{\partial x} \Big|_{x=+0} = \frac{3}{Rm} \left(\frac{h_0}{h_0 + \Delta h} \right)^2, \quad (13)$$

where subscripts ± 0 indicate the difference in right- and left-hand limits for slope in $x = 0$. Thus the SS approach responds to the discontinuity boundary conditions by discontinuity of slope, $\partial h/\partial x$ at $x = 0$ (see SS approach on Figures 4a and 4c at $x = 0$). This result was also illustrated by case 1 from *Royden* [1996], although it was not discussed from this point of view there. Initially, when $\Delta h \sim 0$, the tangent of the slope estimated by the SS approach is $1.5/Rm$, half of the discontinuity across the transition point $x = 0$ (equation (13)). That the slope depends on Rm again illustrates the inconsistency of the SS approach during the initial phase of evolution (compare with section 3.1 which concluded that initial phase of wedge evolution does not depend on Rm).

[28] *Buck and Sokoutis* [1994] presented an analytical solution of a simplified version of the SS model (equation (9)) and predicted an asymptotic averaged slope of $\sim 0.5/Rm$. The simplification includes linearization of equation (9), which is only valid for initial phase (when $h \sim h_0$). As discussed above, however, the SS approach does not predict correctly the initial phase, and the estimation of slope behavior provided by *Buck and Sokoutis* [1994] does not match to actual results. Analysis provided by AM1 and supported by long-time PS runs (up to $t' = 30$) shows that the long-term asymptotic value for the mean slope is 0 and is independent of Rm . However, the characteristic time to approach this value is so large that we cannot expect to examine this limit in nature (characteristic time is tens of millions of years for sediments, or hundreds of millions of years for crust, using Table 2).

3.4. Asymmetry of a Wedge

[29] Consider horizontal forces acting on a complete asymmetric wedge system (Figure 6). The equilibrium of horizontal forces results in the simple condition $F_{\tau+} = F_{\tau-}$, which is the main equation of the second analytical model,

AM2. In order to estimate the basal traction force we assume a parabolic profile of velocity with depth, $(v_x(x, z) = C_2(x)z^2 + C_1(x)z + C_0(x))$, which is predicted by the SS approach. The parameters $C_i(x)$ are determined by the boundary conditions: (1) no slip at the base, and; (2) shear stress free at the top surface, and (3) a linear decrease of the total mass flux from the V^*h_0 at the left toe ($x = \lambda_+$) to 0 at the right toe of the wedge ($x = -\lambda_-$) (Figure 6). The first condition means that the velocity reaches the boundary velocity at the base (0 or $-V^*$, depending on position with respect to the transition point, $x = 0$). The second condition results in $\partial v/\partial z = 0$ at $z = h$, where $h(x)$ is the thickness of the simplified triangular wedge. The third condition means that the wedge is assumed to grow uniformly along its length.

[30] These conditions allow an analytical solution for velocity in the wedge. Integration of the viscous shear stresses along the base of the wedge results in estimates of $F_{\tau+}$ and $F_{\tau-}$, which depend (nonlinearly) on two horizontal length scales, λ_+ and λ_- , the lengths of the two sides of the wedge. Equilibrium of the horizontal forces results in the simple relation between these two length scales:

$$\lambda_- = \frac{\max(h)}{h_0} \lambda_+ = \left(1 + \frac{\Delta h}{h_0} \right) \lambda_+. \quad (14)$$

To a first approximation, the AM2 approach explains wedge asymmetry by more intense resistance from the shear stress

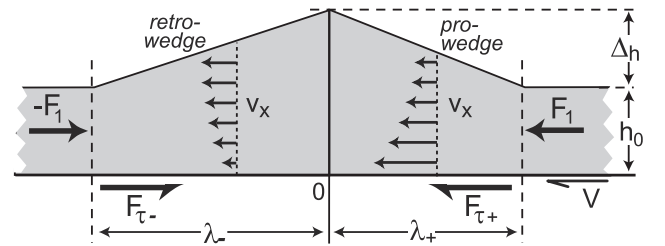


Figure 6. Analysis of wedge asymmetry using AM2. The lateral forces at the toes of the wedge (F_1) are estimated from the lithostatic pressure and are equal in value. A parabolic profile of the distribution of horizontal part of velocity, v_x , with depth is assumed within the wedge.

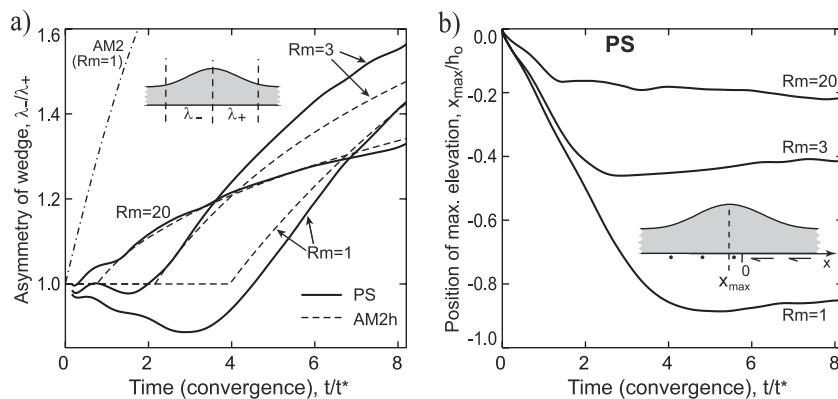


Figure 7. Dependence of the evolution of wedge asymmetry on Rm . (a) Ratio, λ_+/λ_- , of two horizontal length scales of deformation. AM2 approach (dash-dotted line) predicts monotonically increasing asymmetry. PS results have an initial phase with low asymmetry and a second phase with increasing asymmetry. The timescale of these phases and rate of development of asymmetry depend on Rm (see also AM2h approach, equation (15)). (b) PS predicted shift of location of maximum topography (x_{max}) with respect to $x = 0$. This shift is more significant for low Rm (higher viscosity of layer or faster boundary velocity). Note that SS approximation predicts no shift.

in the prowedge than in the retrowedge. The kinematics behind the AM2 approach results in the average velocity, $\bar{v}(x) = F/h$ (where $F(x)$ is the flux across the wedge), which decreases faster in the prowedge (due to increasing thickness) than in the retrowedge (where thickness decreases). This results in $\bar{v} < V/2$ at $x = 0$ in the asymmetric wedge (compare with AM1 where $\bar{v} = V/2$ is used). Shear stress in the prowedge can be estimate as proportional to $V - \bar{v}$, and it is more intense than basal traction in the retrowedge, which is proportional to \bar{v} (basal velocity is 0 there). Thus the length scale of the retrowedge is wider than the prowedge, $\lambda_+ < \lambda_-$, to compensate for difference in intensity of basal stresses.

[31] The purpose of the AM2 approach is not to investigate the complete wedge evolution but to understand sources of the wedge asymmetry. Therefore, unlike AM1, AM2 analysis is not completed here. Instead, the results of the PS numerical calculations are used to check the validity of the inferred causes of asymmetry derived from AM2. Equation (14) predicts that the retrowedge should be the wider from the outset (Figure 7a, AM2). However, the results of PS numerical calculations do not show this behavior at the initial stages, but rather the opposite (Figure 7a, PS, $Rm = 1$).

[32] The results show (Figure 7a) that the evolution of wedge asymmetry can be divided into two phases with certain properties: (1) an initial low-asymmetry phase, which lasts longer for low Rm , and (2) a developed asymmetric phase, in which the asymmetry grows faster for low Rm . The low asymmetry property of the first phase is similar to relationship between the point of maximum mean slope and Rm (Figure 5b), which was revealed by introducing evolution timescale, t_c^* (Figure 5c). The property of the second phase is similar to the AM2 behavior. These properties suggest a hybrid model AM2h in which the evolution of wedge asymmetry is divided into two

phases with different relations between the widths of proside and retrowedge:

$$\begin{aligned} \text{Phase 1 (symmetric, } t'_c < t'_a) \quad \lambda_- &= \lambda_+ \\ \text{Phase 2 (asymmetric, } t'_c > t'_a) \quad \lambda_- &= \lambda_+ + \frac{\Delta_h - \Delta_a}{h_0} \lambda_+, \end{aligned} \quad (15)$$

where $\Delta_a = \Delta_h(t = t_a)$ is the uplift of the wedge at the end of phase 1 and the dimensionless evolution time t'_a separates two phases. The results presented in Figure 7a for AM2h are based on $t'_a = 3.9$ (which can be reformulated via the convergence time as $t_a/t^* = 3.9/\sqrt{Rm}$ using equation (12)). AM2h provides a first-order explanation of the development of asymmetry in the wedge and demonstrates the source of asymmetry during phase 2.

[33] The second asymmetry property is the shift of the point of maximum uplift, x_{max} , from the singularity in the boundary conditions, $x = 0$ (Figure 7b). This parameter also demonstrates a two-phase evolution. During phase 1, x_{max} moves retroward velocity $\sim V/4$, whereas in phase 2, x_{max} is stable or even retreats slightly. The transition time between these phases is well approximated by evolution time $t'_a = 3.9$, the same timescale that applies to the growth of topographical asymmetry (equation (15)).

[34] This property also demonstrates the inaccuracy of thin sheet approximations, which always give $x_{max} = 0$. Although the shift remains relatively small in an absolute sense (e.g., 1/14 of the wedge width for $t' = 8$, $Rm = 1$) and even smaller for $Rm > 1$, this displacement is a characteristic property of wedge growth.

[35] In summary, the development of asymmetry parameters divides wedge evolution into two phases. While the geometry of the second phase is quite understandable and can be modeled by simple approaches (AM2 and SS), the first (initial) phase is less clear and requires more investigation.

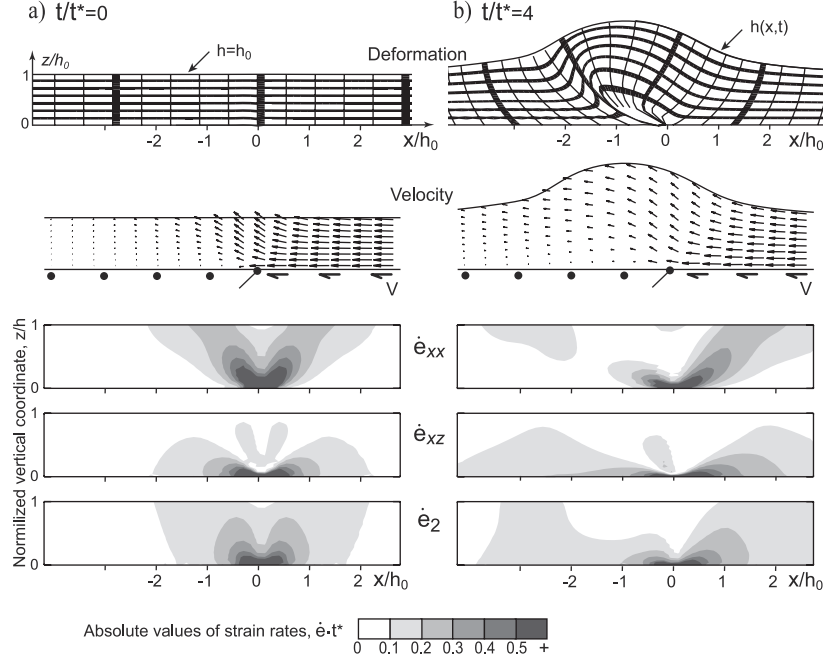


Figure 8. Internal mechanics in an $Rm = 1$ PS wedge at two phases. From top to bottom, deformations of passive marker lines (with undeformed markers shown on the left); velocity field (arrows) and boundary conditions; contour plots of absolute values of horizontal strain rate, $\dot{\epsilon}_{xx}$; shear strain rate, $\dot{\epsilon}_{xz}$; and second invariant of strain rate tensor, $\dot{\epsilon}_2$. Note that the three bottom panels are scaled by thickness of wedge, which maps the wedge to a rectangle of dimensionless thickness 1.

3.5. Internal Deformation

[36] The distributions of internal mechanical fields illustrate the differences between two consecutive stages of PS wedge evolution (Figure 8). For $t' \approx 0$ (Figure 8a) the style is a “plug” mode with two conjugate high horizontal strain rate, $\dot{\epsilon}_{xx}$, zones. The relatively low deformed central part of the embryonic wedge moves up and retoward, preserving symmetry at the surface. Thus the plug mode is compatible with two features of the initial phase asymmetry described in section 3.4 (length scales ratio and the shift of point of maximum uplift, Figure 7). This mode occurs for all Rm at the initial stages and persists longer for low Rm , similar to the phases of asymmetry. For $t' = 4$ (Figure 8b), deformation is no longer symmetric and the $\dot{\epsilon}_{xx}$ focused compressional zone in the retorside is diminished.

[37] The simple rheological model allows the strain rate contours to be converted to stresses $\tau_{ij} = 2\mu\dot{\epsilon}_{ij}$, where τ_{ij} are the components of the viscous stress tensor. For $Rm = 1$ (Figure 8) the viscous stress in some parts of wedge (black area, Figure 8) is higher than the characteristic gravitational stress $\sigma_g^* = \rho gh_0$ (Table 1). Following *Medvedev and Podladchikov* [1999a], the total pressure in the system can be approximated dimensionally and [dimensionless] as

$$\begin{aligned} P(x, z) &\approx \rho g(h - z) - 2\mu\dot{\epsilon}_{xx} \\ [P'(x', z') &\approx Rm(h' - z') - 2\dot{\epsilon}'_{xx}] \end{aligned} \quad (16)$$

and the dynamic (viscous) part of the pressure can exceed the lithostatic part of pressure for low Rm especially at the

initial stages (Figure 8a, see also *Petrini and Podladchikov* [2000]). During later stages the relative influence of the dynamic part decreases owing to defocusing of the high strain rates zones (Figure 8b) and increasing lithostatic pressure as the wedge grows (equation (16)).

[38] The PS results (Figure 8) also provide a way of estimating the forces used to build the AM1 approach (equations (2) and (3)). The normal viscous force, F_n , is estimated by integrating the viscous stress $2\mu\dot{\epsilon}_{xx}$ in the vertical direction at $x = 0$. The contours show significant strain rate variations and, therefore, stress variations along this integration path at time $t' = 0$, while by time $t' = 4$ these stress variations have decreased significantly. The basal shear, F_τ , results from integrating the shear stress along the base from $x = 0$ over the region of active shear. Contours for $\dot{\epsilon}_{xz}$ change much less with time, a property that is used in section 4.2.

4. Evolution of the Surface Deformation

[39] *Buck and Sokoutis* [1994] pointed to the existence of regions of surface extension in viscous wedges subjected to compression by basal traction. Aspects of this behavior can be explained by using the approaches discussed earlier in which the surface strains are measured by the change in length, $\ell(x_0, t)$, of small Lagrangian segments of the upper surface:

$$\varepsilon(x, t) = (\ell(x_0(x, t), t) - \ell_0) / \ell_0 \quad (17)$$

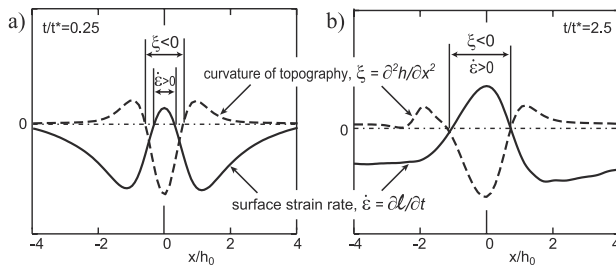


Figure 9. Comparison of regions of positive surface strain rates ($\dot{\epsilon} > 0$) and regions with negative surface curvature ($\xi = \partial^2 h / \partial x^2 < 0$) using the PS model. The correlation predicted by the SS approach is poor for initial phase (Figure 9a), but improves later (Figure 9b). Thus negative curvature is a predictor of surface extension after finite growth. Vertical scale is arbitrary.

where ℓ_0 is the initial length of the small segment. This approach differs from that used by *Willett* [1999], who only take horizontal changes into account. The main difference is seen in the extension for low Rm , which can be negligible when only the horizontal component is used.

4.1. Surface Strain Rates

[40] A necessary condition for finite surface extension is an extensional strain rate along the surface. Variations of surface strain rates for conditions similar to those presented here and for different rheologies and boundary conditions are given by *Royden* [1996] and *Willett* [1999]. Here we emphasize only one property of the surface ($z = h$) strain rates derived from the SS approach (equation (8)):

$$\dot{\epsilon}_{xx}|_{z=h} = \frac{\partial v'(x, h)}{\partial x} = -Rm \frac{(h')^2}{2} \frac{\partial^2 h'}{\partial (x')^2} - Rm h' \left(\frac{\partial h'}{\partial x'} \right)^2, \quad (18)$$

which shows that the SS approach predicts extensional strain rate ($\dot{\epsilon}_{xx} > 0$) only if the curvature of the upper surface is negative ($\partial^2 h / \partial x^2 < 0$). Given that the second term of (equation (18)) is of second order for low slopes, the SS model directly relates extensional strain rate regions to zones with negative curvature of topography.

[41] A test of this SS prediction using the complete PS approach (Figure 9) shows a poor correlation of extension and curvature initially (Figure 9a), which is explained by the strong initial influence of the normal compressive stresses that are ignored in SS. The results of Figure 9b and, corresponding results for different Rm and time, exhibit a good correlation. Therefore negative curvature is a first-order predictor of the location of extensional surface strain rates in wedges beyond the initial growth phase.

[42] The SS approach is also inaccurate in estimating surface strain rates above $x = 0$. This is because the discontinuity in the horizontal derivative of layer thickness at $x = 0$ (equation (13)) results in a discontinuity of surface strain rate (equation (18), see also *Buck and Sokoutis* [1994]). The discontinuity is an artifact that is caused by the failure of the SS model to handle correctly the discontinuous boundary conditions. Failure

to recognize this artifact of the SS approach in modeling surface strain rates can lead to the mistaken interpretation of this discontinuity as an extensional regime (see, for example, the misinterpretation in *Royden's* [1996, Figure 5] case 1).

4.2. Finite Surface Strains

[43] In AM1, symmetric wedge behavior is considered in terms of the balance of three main forces which also determine the surface strains. Considering surface deformation, we will not take into account basal traction, F_τ , which does not affect surface strains directly because the the surface is free of shear stress. F_n integrates the normal viscous stress responsible for compression along the horizontal axis. The gravitational force, F_g , acts to spread the wedge horizontally, which can lead to extension on the top surface. The evolution of the force balance in the wedge (Figure 10a) estimated by the AM1 approach (see section 2.1) shows that gravitational force starts at 0 and grows with time while the normal viscous force decreases. After a certain time the gravitational force dominates.

[44] In Figure 10b the wedge evolution predicted by AM1 is divided into domains depending on Rm , thereby outlining which of the forces (F_n or F_g) dominates. Extension is expected when $F_g > F_n$. Although the AM1 approach is highly simplified, it predicts an onset of extension in good agreement with the complete PS results (compare solid line and dots on Figure 10b), which gives credence to the assumptions used in the AM1 model. These results clearly imply that surface extension is driven by the gravitational force, while the initial delay in the onset of surface extension is due to the strong influence of normal viscous stress during initial stages of evolution.

[45] The finite surface strains, calculated from the deformation of surface Lagrangian PS elements (Figure 11), show that both intensity (Figure 11a) and the width of zones of extension (Figure 11b) increase with increasing Rm . Note that *Willett* [1999] used only horizontal strains and therefore his results for low Rm wedges, with high slope and low-amplitude extension, differ from complete surface strains used here. Long-time PS results for low Rm (Figure 11a)

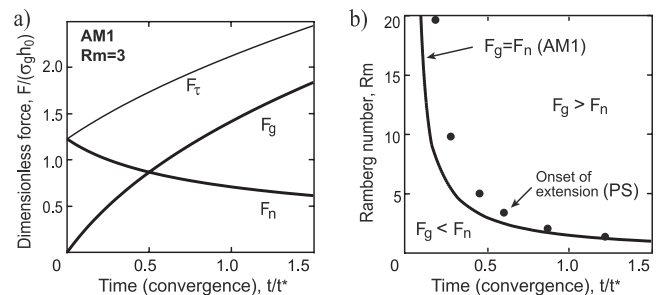


Figure 10. Analysis of the evolution of averaged forces (F_n , F_g , F_τ) in the wedge and their relation to surface strains. (a) AM1 balance of forces. F_g and F_n evolve in opposite directions, and F_g dominates over F_n after some time. (b) Results of PS modeling (dots) showing that finite extension appears at the surface shortly after F_g exceeds F_n (solid line).

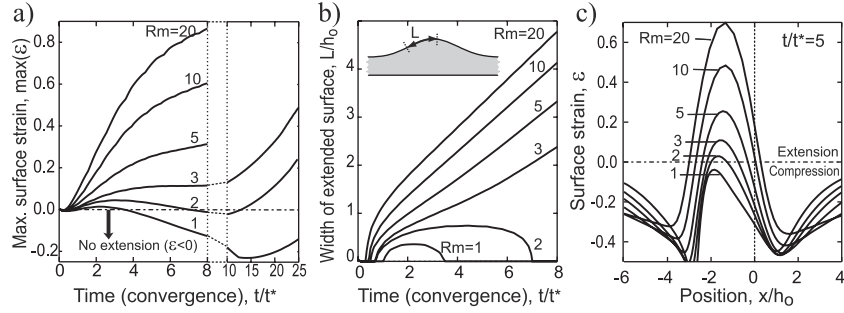


Figure 11. Analysis of PS finite surface strain (equation (17)) for different Rm . (a) Evolution of maximum surface strain (intensity of extension). When the maximum strain is negative (e.g., for $Rm = 1$ for $t' > 3.5$), there is no finite extension. (b) Evolution of the width, L , of the region exhibiting finite surface extension. (c) Finite surface strain distribution at time $t' = 5$ for different Rm .

indicate a temporary disappearance of surface extension, which will be discussed in section 4.3.

4.3. Incremental Surface Strains

[46] In addition, it is important to investigate how strains of the surface Lagrangian elements evolve with time. *Willett* [1999] explained several features by roughly considering this evolution. Here we provide a more systematic analysis based on the example of of an $Rm = 2$ wedge.

[47] There are four types of surface elements (Figure 12) characterized by different extension/contraction histories, and this division depends on initial position of the elements. Type 1 elements initially located in the retroside ($x_0 < 0$, e.g., elements 1 and 1' on Figure 12) gradually contract and never exhibit intervals of extension. Type 2 elements initially located in the proside ($x_0 > 0$, e.g., element 2 on Figure 12) undergo an interval of extension following a short period of compression. Even though points 1' and 2

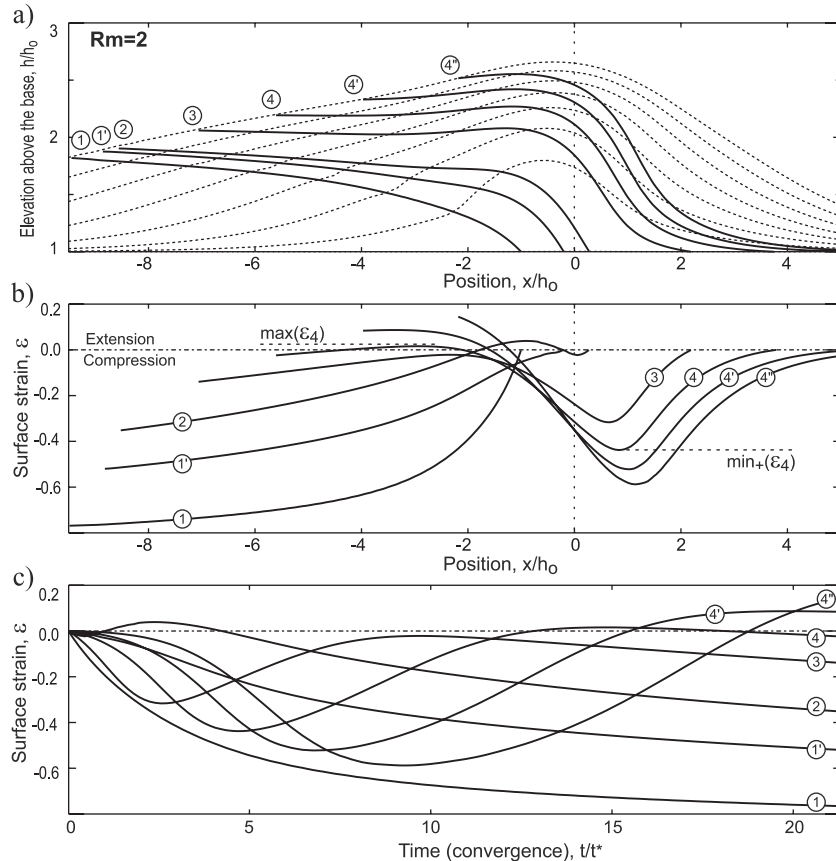


Figure 12. Evolution of small Lagrangian surface segments for an $Rm = 2$ PS wedge. (a) Motion of the segments (solid lines) as topography (dashed lines) evolves ($t' = 3, 6, \dots, 21$). (b) Evolution of the surface strains, $\epsilon_i(t')$, of the segments as they are translated horizontally. (c) Evolution of surface strains of the segments with time (t').

are initially located close to each other (Figure 12a), their strain evolution differs significantly (especially during the initial stages). The initial position of element 2 inside the plug (similar to the one described for $Rm = 1$ on Figure 8) results in almost no initial compression, and further uplift stretches this segment giving finite extension (Figures 12b and 12c).

[48] Type 3 Lagrangian segments (e.g., element 3 on Figure 12) are located within the initial compressional zone (Figure 8, $\dot{\epsilon}_{xx}$). This results in early fast and intensive contraction. The later stage of extension is insufficient to offset the contraction, and this type of segment never exhibits finite extension (Figures 12b and 12c). When type 3 elements dominate the wedge surface, replacing the type 2 (e.g., $t' = 6 \dots 9$, Figure 12a), the zone of finite extension disappears.

[49] As the wedge grows, the relative influence of the compressional zones decreases, and zone of instantaneous extension surrounding the maximum uplift becomes more significant. This results in the reappearance of the zone of the finite extension for the type 4 Lagrangian surface segment (e.g., segments 4, 4', and 4''). These segments were initially located far from the point $x = 0$. They accumulate a significant amount of surface-parallel shortening but enter the central part of wedge late when the gravitational spreading becomes dominant. Superposition of cumulative extension results in finite extension (Figures 12b and 12c), which distinguishes type 4 segments from type 3.

[50] Unlike $Rm = 2$ (Figure 12), wedges with $Rm > 2.5$ have lower-intensity and shorter-duration contractional zones, and type 3 Lagrangian segments no longer occur. For such wedges, there are only two types of surface strain evolution corresponding to types 1 and 4.

[51] The relationship between zones of instantaneous and finite surface strains is illustrated by segment 4 (Figure 12). Prior to $t'_1 \sim 4.5$ (Figures 12b and 12c) this segment is shortened in the proside compressional zone. It is then advected into the extending zone and gradually increases its length between t'_1 and $t'_2 \sim 15$. It then enters the retroside compressional zone, and the length again decreases. Thus the strain at $t' = t'_2$ records the maximum cumulative extension of the segment. This evolutionary path demonstrates why finite extension is found mainly on the retroside (see Figure 11c) despite the almost symmetric distribution of the zone of instantaneous extension about the maximum uplift in the system ($x_{\max} \sim 0.5$). Figure 12a also illustrates the conclusion of the section 4.1 because segment 4 is located on the part of the topography with visible negative curvature for $t' = 6, 9, 12$, which spans the time when it is subjected to extension (Figure 12c).

[52] The evolution of Lagrangian elements can be generally characterized by several parameters: the evolution of the absolute maximum of the strain (Figure 11a) and the incremental extension $\Delta\epsilon = \max(\epsilon_i) - \min_+(\epsilon_i)$ (subscript + here refers to the proside compressional zone, Figure 12b), which illustrates the maximum superimposed extension of segment i regardless of the initial contraction in the proside compression zone ($\min_+(\epsilon_i)$), evaluated over all wedge elements as a function of time and Rm (Figure 13). The results demonstrate that for high Rm the zone of extension can stretch the surface segments by up to 100% of their initial length ($\Delta\epsilon > 1$ for $Rm = 20$). This parameter

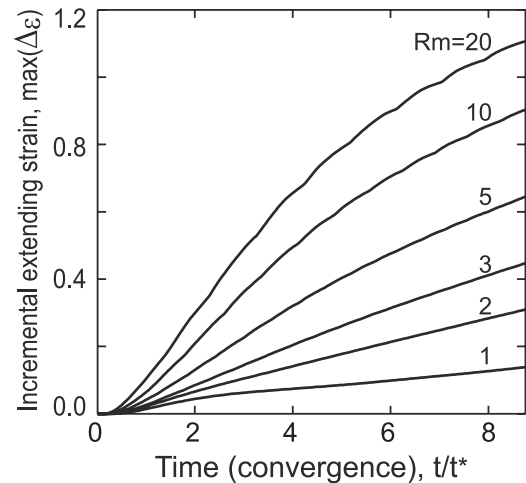


Figure 13. Evolution of maximum incremental extension of Lagrangian surface segments, $\max(\Delta\epsilon)$, for different Rm . $\Delta\epsilon$ is calculated for each surface segment as difference between its maximum strain, $\max(\epsilon_i)$, and minimum strain acquired in the proside compressional zone, $\min_+(\epsilon_i)$ (Figure 12b); and the maximum among all segments is plotted depending on time.

grows with time and can reach high values even for low Rm (e.g., segment 4'' exhibits $\Delta\epsilon = 0.15 - (-0.6) = 0.75$ at $t' = 22$, Figure 12c).

[53] The results presented in this section demonstrate that surface strains accumulate in an asymmetric way during advection. The total strain tends to be dominated by the proside contraction as shown by the PS model. The simplifications behind the AM1 approach ($\lambda_+ = \lambda_-$ and complete symmetry of the sides in regard to advecting material) do not take into account these asymmetries, and this explains why AM1 fails to accurately predict the relation between forces and strains in wedges with low Rm . In contrast, the SS approach predicts better the evolution of finite surface strains, as was demonstrated by results of *Buck and Sokoutis* [1994].

5. Discussion and Conclusions

5.1. Evolutionary Phases of Viscous Orogenic Wedges

[54] As predicted by the scaling analytical model AM1 and supported by numerical calculations (Figure 5), the evolution of viscous wedges is not linear and can be divided into three phases. Figure 14 separates these phases by their different styles of wedge growth comparing rates of thickening and widening the wedge and introducing zones A and C that separate the three phases and zone B with self-similar growth of the wedge (see Figure 14 caption for details). There are also several features that differentiate phases.

[55] Phase one is characterized by mostly vertical, plug-like (Figure 8a), growth of the wedge above the zone of transition in boundary conditions ($x = 0$, where the basal velocity changes). This phase can be described as geometric since the evolution is relatively insensitive to the rheology and boundary velocity (Figures 3a and 3b). The main forces during this period are horizontal viscous, F_n , and basal shear, F_τ (Figure 10).

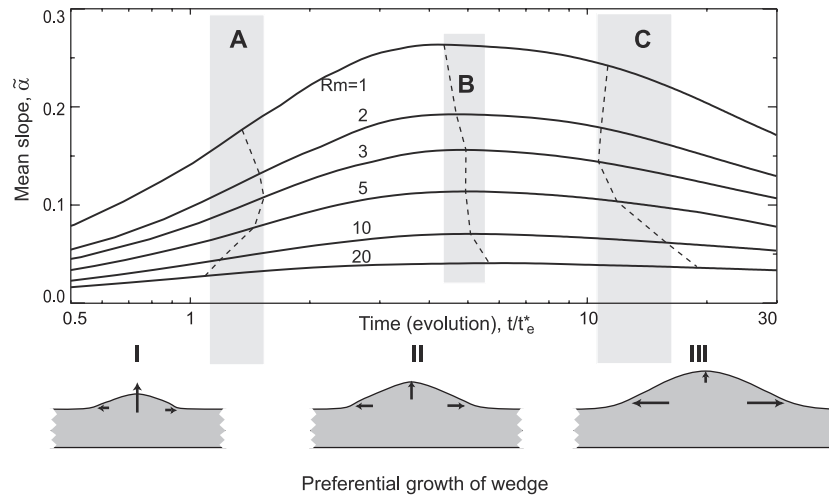


Figure 14. Phases of viscous wedge growth demonstrated by the evolution of mean slope, $\tilde{\alpha}$ (equation (11)). The three phases are I, initial, growth is mostly vertical; II, developed, growth is close to self-similar; and III, final, the wedge spreads horizontally. The size of arrows on bottom panels illustrates these relative styles. These stages are separated by the asymptotic behavior of the growth of Δ_h and λ with time. The mass balance (equation (6)) relates these parameters and the convergence time as ($\Delta_h' \lambda' = 2t'$), which can be rewritten as proportional relation ($\Delta_h' \lambda' \propto t'$). Thus, if growth of the maximum elevation scales with time as ($\Delta_h' \propto (t')^\beta$), the deformations width scales as ($\lambda' \propto (t')^{(1-\beta)}$). During the initial phase, $\Delta_h \propto t'$ and $\beta \approx 1$, while $\lambda \approx \text{const}$. Parameter β decreases with evolution of wedge. Zone A separates the first and second phases with the condition $\beta \approx 0.83$. Zone B represents self-similar growth of the wedge with $\beta \approx 0.5$ (note also that condition $\beta = 0.5$ is equivalent to condition of maximum mean slope). Zone C indicates the onset of the third phase with $\beta \approx 0.4$. In each of these zones (A, B, and C) the exact match to the parameter value ($\beta = 0.83, 0.5$ and 0.4 correspondingly) is shown by the dashed line.

[56] Phase two is transitional and is marked by a change in the orientation of preferred growth from vertical to horizontal (with some period of close to self-similar growth, zone B on Figure 14) and by a change of the style of asymmetry development (the separation point between two phases of asymmetry development estimated in section 3.4 (Figure 7) is located in proximity to the zone B on Figure 14). One of the main characteristics of this phase is the onset of finite surface extension. The gravitational potential energy grows during the initial phase such that all three forces described in the AM1 approach (equation (3)) become important in phase 2 (Figure 10a).

[57] Although the wedge grows continuously, the mean slope of the wedge decreases during the third phase. The influence of the normal horizontal viscous stress decreases asymptotically during this phase, and the evolution is driven by the equilibrium between gravitational spreading and shear traction along the base. By analogy with the model of wedge evolution presented by Platt [1986], phase 3 can be described as underthrusting (underplating).

[58] Along with the dimensionless convergence time (Table 1), the evolution time was introduced (equation (12)). The latter parameter includes rheological and boundary conditions of wedge evolution, and it demonstrates the scaling between the real time of evolution and the phases of evolution (Figure 14). Equation (12) shows also that a wedge evolves through these phases faster if it is characterized by relatively lower viscosity and/or higher convergence velocity and/or higher density.

[59] Feehan and Brandon [1999] present a conceptual model of different modes of steady state accretionary

wedges: “thickening” (described by mainly surface contraction), “mixed,” and “thinning” (described by significant surface extension). The properties of these modes are linked to the three phases presented here: the first phase of wedge evolution is characterized by both rapid thickening and surface compression; the third (final) stage is characterized mainly by widening of the wedge and broadening the zone of finite surface extension; the transition phase has mixed characteristics of the two end phases. Thus the modes of steady state wedges described by Feehan and Brandon [1999] can be a result of reaching the stationary states at different phases of wedge evolution.

5.2. Variations on the Simple Model

[60] The problem considered in this study is highly simplified, and direct application of the results to tectonic wedges may be limited. However, analyzing the simple model can help to understand and even predict some results of variations of this model or more complicated models.

[61] The boundary conditions used in this study to model the wedge evolution include a discontinuity in basal velocity at the point $x = 0$ (Figure 1a) or a corresponding rapid transition in the PS models. This kind of boundary condition corresponds to asymmetric basal subduction or underthrusting. Although it results in significant simplification of the analytical models, other boundary conditions may also prevail. We have also investigated several numerical PS models in which the basal boundary velocity is a continuous function with broad transition. The results are qualitatively similar to those described earlier. Moreover, the AM1 approach can be extended to models with finite

Table 3. Model Approaches Used in This Study and Their Interrelationships^a

Model	Influenced by			
	AM1	AM2 (AM2h)	SS	PS
AM1 (analytical model 1: scaling analysis of forces, section 2.1)	estimates evolution of the most general parameters (has analytical solution)		supports conclusions on evolution of the mean slope (Figure 5)	controls applicability of the approach
AM2 (analytical model 2: kinematic approach to force balance, section 3.4)	shows a need in velocity profile to describe asymmetry of wedge	estimates asymmetry of wedges (has analytical solution)	similar analytical resolving of the vertical profiles of the velocity field	controls applicability of the approach
SS (simple shear: thin sheet approximation, section 2.2)	shows possible applicability of thin sheet approximation to the problem and outlines limitations of the SS approach during the initial stages	parabolic dependence of velocity with depth defined by topography describes initial stage of evolution incorrectly	numerical simulations based on approximate solution of depth dependence	outlines applicability of the method; Rm and time dependence of accuracy (Figure 4)
PS (plane strain: complete numerical model, section 2.3), evolution of the wedge	outlines phases of wedge evolution (Figure 5), introduces dimensionless time of evolution (equation (12)) speculative explanation of finite surface extension (Figure 10)	gives insights into the first phase of evolution, and estimates evolution of asymmetry during the later stages (Figure 7)	estimates surface extension [Buck and Sokoutis, 1994], relates surface curvature and surface strain rate (Figure 9)	acts as reference model, to test and support conclusions of this study

^aThe model column presents the approaches and their general descriptions. The underlined diagonal cells outline aims of each approach. The PS row outlines results of applications of different approaches by comparing with the reference PS approach.

width transition zones, and the same three-phase evolution is predicted because the relationships among three driving forces evolve in the same manner. Our recent numerical experiments [Medvedev *et al.*, 2000] show that the crustal wedge with local (Airy) isostasy evolves with the same, three-phase, pattern. The evolution of the wedge taper (the analogue of the mean slope in this case) corresponds closely to the results presented in Figure 5 if Rm is scaled by the isostatic amplification factor ($\Phi = 1 - \rho/\rho_m$, where ρ_m is the density of mantle).

[62] The link between the superposition of average forces and surface extension presented by the AM1 approach (Figure 10) can be extended to Coulomb wedges. In critical tapered Coulomb wedges, horizontal stresses are always higher than vertical stresses [Dahlen, 1990], and no finite surface extension can be expected according to AM1. This supports conclusions made by Willett [1999].

5.3. Relations Among the Different Approaches

[63] The interrelationships among the analytical and numerical models used here is summarized in Table 3. The purpose of Table 3 is to show what aspects of the complete solution are predicted by the analytical models and the insights concerning scaling and phases of the evolution that can be derived from the analytical models.

[64] The relative strengths and weaknesses of the models can also be compared. For example, the AM1 approach models the initial phase of wedge evolution with good accuracy (Figure 5). Why then is the more sophisticated AM2 approach unable to model this phase with any accuracy? The difference is that AM1 averages forces acting in the wedge to a much higher extent than AM2, for example, estimating shear stress by averaging over the thickness of the entire layer. AM2 assumes a particular form of the distribution of velocities inside the wedge and

bases the whole analysis on this assumption. Comparison of AM1 and AM2 leads to the conclusion that the shear stress is indeed the driving force but that velocities are not uniform inside the wedge. This insight leads to the idea of the initial phase in the form of a plug with deformation accommodated within the bounding compressional zones. This mode is both predicted by the PS approach and easily examined by this technique (Figure 8).

[65] An additional important result is that thin sheet approximations can lead to inaccurate results for the problem described here. Even the AM approaches give superior results for some cases. The PS approach provides an accurate two-dimensional vertical cross-section model and allows the approximations of the other methods to be avoided. In three dimensions, however, the full numerical solution is computationally expensive and the use of thin sheet approximations is one of the few simple alternatives. Nevertheless, the limitations of the SS approach described here are fundamental and must be taken into account.

5.4. Cautions Concerning Comparisons With Natural Wedges

[66] Several parameters introduced here allow observations from natural wedges to be linked to the bulk viscosity of the model wedges. These links, however, are not linear, and the parameters should be analyzed with caution.

[67] The mean slope, $\tilde{\alpha}$, introduced in section 3.3 can be easily estimated for natural wedges. However, the analysis described here shows that this parameter cannot be directly related to bulk viscosity and/or Rm . Unlike the taper for critical Coulomb wedges, the parameter $\tilde{\alpha}$ is time-dependent. For example, $\tilde{\alpha}$ can characterize wedge with $Rm = 2$ at dimensionless time 3 and $Rm = 1$ at time 30 (Figure 5).

[68] Section 3.4 introduces two parameters of asymmetry, λ_+/λ_- and x_{\max} . The first parameter, the ratio of proward/

retoward length scales, shares properties of the mean slope: it can be directly estimated from topography of natural orogens, and it is time-/phase-dependent. Figure 7a shows that model wedges with different bulk rheologies can be characterized by the same value of λ_+/λ_- .

[69] The second asymmetry parameter, the shift of the point of maximum uplift, x_{\max} (Figure 7b), can be estimated from the comparison of the topography with the seismicity distribution in active orogens [e.g., Cahill and Isacks, 1992]. Two characteristics of this parameter make it important: (1) after a short initial phase it reaches stable value directly related to Rm ; and (2) this parameter is a distinct characteristics of viscous wedges because frictional-brittle wedges result in $x_{\max} \sim 0$ for wedges with the same boundary conditions [Vanderhaeghe et al., 1998; Willett, 1999].

[70] The parameters of surface extension discussed in section 4 can be compared with distribution of normal faults often observed along the natural wedges. The strain history of surface segments considered in section 4.3 clearly illustrates the zonation of surface strains in orogens. These predictions can be tested by well-established methods of structural geology [e.g., Ramsay and Huber, 1983].

[71] Although each parameter separately cannot provide unique link between observations and the model, the set of parameters presented can draw a clear picture of bulk rheology and dynamic conditions of natural wedges. Once the simple model described here becomes clear, more complicated models can be built and tested using the similar pattern of descriptive parameters.

[72] **Acknowledgments.** This work would be impossible without generous help from other members of Dalhousie Geodynamics Group: Chris Beaumont suggested the problem and significantly improved the presentation and structure of the manuscript; Olivier Vanderhaeghe suggested several topics for consideration; Philippe Fullsack provided his code and helped with the PS approach. This collaboration allows me to use “we” throughout the paper, although any of the errors are mine only. Comments by Djordje Grujic and two anonymous reviewers were helpful. Thomas Funck is thanked for help in preparation of figures. Research was funded by an NSERC research grant to C. Beaumont.

References

- Beaumont, C., P. Fullsack, and J. Hamilton, Styles of crustal deformation caused by subduction of the underlying mantle, *Tectonophysics*, 232, 119–132, 1994.
- Beaumont, C., P. J. J. Kamp, J. Hamilton, and P. Fullsack, The continental collision zone, South Island, New Zealand: Comparison of geodynamical models and observations, *J. Geophys. Res.*, 101, 3333–3359, 1996.
- Beaumont, C., J. A. Muñoz, J. Hamilton, and P. Fullsack, Factors controlling the Alpine evolution of the central Pyrenees inferred from a comparison of observation and geodynamical models, *J. Geophys. Res.*, 105, 8121–8145, 2000.
- Buck, W. R., and D. Sokoutis, Analogue model of gravitational collapse and surface extension during continental convergence, *Nature*, 369, 737–740, 1994.
- Cahill, T., and B. L. Isacks, Seismicity and shape of the subducted Nazca Plate, *J. Geophys. Res.*, 97, 17,503–17,529, 1992.
- Cuvelier, C., A. Segal, and A. A. Steenhoven, *Finite Element Methods and Navier-Stokes Equations*, 483 pp., D. Reidel, Norwell, Mass., 1986.
- Dahlen, F. A., Critical taper model of fold-and-thrust belts and accretionary wedges, *Annu. Rev. Earth Planet. Sci.*, 18, 55–99, 1990.
- Ellis, S., Forces driving continental collision: Reconciling indentation and mantle subduction tectonics, *Geology*, 24, 699–702, 1996.
- Ellis, S., P. Fullsack, and C. Beaumont, Oblique convergence of the crust driven by basal forcing: Implication for length-scales of deformation and strain partitioning in orogens, *Geophys. J. Int.*, 120, 24–44, 1995.
- Ellis, S., C. Beaumont, R. Jamieson, and G. Quinlan, Continental collision including a weak zone—The vise model and its application to the Newfoundland Appalachians, *Can. J. Earth Sci.*, 35, 1323–1346, 1998.
- Emerman, S. H., and D. L. Turcotte, A fluid model for the shape of accretionary wedges, *Earth Planet. Sci. Lett.*, 63, 379–384, 1983.
- England, P., and D. McKenzie, A thin viscous sheet model for continental deformation, *Geophys. J. R. Astron. Soc.*, 70, 295–321, 1982.
- Feehan, J., and M. Brandon, Contribution of ductile flow to exhumation of a thrust wedge, San Juan–Cascade nappes, NW Washington State, *J. Geophys. Res.*, 104, 10,883–10,902, 1999.
- Fullsack, P., An arbitrary Lagrangian-Eulerian formulation for creeping flows and applications in tectonic models, *Geophys. J. Int.*, 120, 1–23, 1995.
- Jones, C. H., J. R. Unruh, and L. J. Sonder, The role of gravitational potential energy in active deformation in the southwestern United States, *Nature*, 381, 37–41, 1996.
- Lobkovsky, L. I., and V. I. Kerchman, A two-level concept of plate tectonics: Application to geodynamics, *Tectonophysics*, 199, 343–374, 1991.
- Medvedev, S. E., Computer simulation of sedimentary cover evolution, in *Computerized Basin Analysis: The Prognosis of energy and Mineral Resources*, edited by J. Harff and D. F. Merriam, pp. 1–10, Plenum, New York, 1993.
- Medvedev, S. E., and Y. Y. Podladchikov, New extended thin sheet approximation for geodynamic applications I, Model formulation, *Geophys. J. Int.*, 136, 567–585, 1999a.
- Medvedev, S. E., and Y. Y. Podladchikov, New extended thin sheet approximation for geodynamic applications, II, 2D examples, *Geophys. J. Int.*, 136, 586–608, 1999b.
- Medvedev, S., C. Beaumont, O. Vanderhaeghe, P. Fullsack, and R. A. Jamieson, Evolution of continental plateaus: Insights from thermal-mechanical modeling (abstract), *Eos Trans. AGU*, 81(48), Fall Meet. Suppl., Abstract T52B-17, 2000.
- Petrini, K., and Y. Podladchikov, Lithospheric pressure-depth relationship in compressive regions of thickened crust, *J. Metamorph. Geol.*, 18, 67–78, 2000.
- Platt, J. P., Dynamics of orogenic wedges and the uplift of high-pressure metamorphic rocks, *Geol. Soc. Am. Bull.*, 97, 1037–1053, 1986.
- Platt, J. P., Mechanics of oblique convergence, *J. Geophys. Res.*, 98, 16,232–16,256, 1993.
- Platt, J. P., Calibrating the bulk rheology of active obliquely convergent thrust belts and forearc wedges from surface profiles and velocity distributions, *Tectonics*, 19, 529–548, 2000.
- Ramberg, H., *Gravity, Deformation and the Earth's Crust*, 2nd ed., 452 pp., Academic, San Diego, Calif., 1981.
- Ramsay, J. G., and M. I. Huber, *The Techniques of Modern Structural Geology*, vol. 1, *Strain Analysis*, 307 pp., Academic, San Diego, Calif., 1983.
- Ring, U., M. T. Brandon, Ductile strain, coaxial deformation and mass loss in the Franciscan complex: Implications for exhumation processes in subduction zones, in *Exhumation Processes: Normal Faulting, Ductile Flow and Erosion*, edited by U. Ring et al., *Geol. Soc. Spec. Publ.*, 154, 55–86, 1999.
- Royden, L., Coupling and decoupling of crust and mantle in convergent orogens: Implications for strain partitioning in the crust, *J. Geophys. Res.*, 101, 17,679–17,705, 1996.
- Schlichting, G., *Boundary-Layer Theory*, 7th ed., McGraw-Hill, New York, 1979.
- Shen, F., L. H. Royden, and B. B. Clark, Large-scale crustal deformation of the Tibetan Plateau, *J. Geophys. Res.*, 106, 6793–6816, 2001.
- Vanderhaeghe, O., C. Beaumont, P. Fullsack, S. Medvedev, and R. A. Jamieson, Thermal-mechanical modelling of convergent orogens: The role of rheology, isostasy and temperature, in *ECSSOOT 73rd Transect Meeting*, edited by R. Wardle and J. Hall, 44–85, Lithoprobe Secretariat, Vancouver, B. C., Canada, 1998.
- Weijermars, R., and H. Schmeling, Scaling of newtonian and non newtonian fluid dynamics without inertia for quantitative modelling of rock flow due to gravity (including the concept of rheological similarity), *Phys. Earth Planet. Inter.*, 43, 938–954, 1986.
- Willett, S. D., Rheological dependence of extension in wedge models of convergent orogens, *Tectonophysics*, 305, 419–435, 1999.
- Zanamonetz, V. B., V. O. Mikhajlov, and V. P. Myasnikov, Mechanical model of block folding formation, *Phys. Solid Earth*, 12, 631–635, 1976.
- Zienkiewicz, O. C., and R. L. Taylor, *The Finite Element Method*, 4th ed., 1400 pp., McGraw-Hill, New York, 1989.